Dalton Transactions

ROYAL SOCIETY OF CHEMISTRY

PAPER

View Article Online
View Journal | View Issue

Cite this: *Dalton Trans.*, 2023, **52**, 7196

Evaluation of triphenylene-based MOF ultrathin films for lithium batteries†

Isabel Ciria-Ramos, [a,b] Inés Tejedor, [a,b] Lucía Caparros,[a,b] Beatriz Doñagueda, [a,b] Oscar Lacruz,[a,b] Ainhoa Urtizberea, [a,c] Olivier Roubeau, [a] Ignacio Gascón [a,b] and Marta Haro *[a,b]

Metal–organic frameworks (MOFs) are attractive candidates to meet the requirement of next-generation batteries, as functional materials with a high surface area, well-defined metal centers, and organic linkers through coordination bonds. Due to their great tunability, MOFs have been investigated as electrodes or electrolytes in lithium batteries and more recently as protective layers in anode-less batteries. Here, we synthesize a $Ni_3(HHTP)_2$ MOF directly at the air–liquid interface of a Langmuir trough and grow the electrode on a conductive substrate by the transference process. The characterization during Langmuir film formation shows that the addition of crystallization time during the compression process enhances the formation of 2D crystalline domains, as observed by *in situ* grazing-incidence X-ray diffraction. Next, the transferred $Ni_3(HHTP)_2$ ultrathin films were studied as working electrodes in Li batteries in a half-cell configuration and compared with bare copper. The results show that the $Ni_3(HHTP)_2$ film protects the Cu collector from oxidation, and the negative charge accumulates in the organic ligand during the lithiation process while Ni^{II} oxidizes to Ni^{III}, unlike other triphenylene-based MOFs with Cu^{II} or Co^{II} metal nodes. The galvanostatic plating–stripping cycles of the batteries show that the inclusion of the crystallization time improves the coulombic efficiency, especially significantly in the first cycles when the SEI is formed. This work shows the Langmuir technique as a useful tool to test MOF based materials for batteries with the advantages of using a low amount of raw materials and without the need to introduce additives (binder and electron conductor) in the electrodes. The electrochemical study of this type of electrode allows a first screening to synthesize electrodes based on MOFs and can be a tool for the preparation of protective coatings under optimized conditions.

Received 22nd March 2023,
Accepted 27th April 2023

DOI: 10.1039/d3dt00876b

rsc.li/dalton

1. Introduction

Metal–organic frameworks (MOFs) are a subset of coordination networks extending in either two or three dimensions, composed of inorganic nodes (clusters or metal ions) connected by organic ligands and containing potential voids.[1] Although most MOFs are crystalline and exhibit permanent porosity,[2] there are also amorphous MOFs, MOF liquids, MOF glasses, and non-porous MOFs.[3] Due to their rational design, structural diversity, and tunable physical and chemical properties (including surface area, pore size, functionalities, *etc.*), MOFs have been intensively studied as advanced functional materials for a large variety of applications,[4] including environmental remediation processes,[5] CO_2 capture,[6] and energy storage.[7] In the particular case of lithium batteries, MOFs are scarcely used compared to inorganic or graphitic materials and most of the studies employ them as the template or precursor of carbon based electrodes because of the low MOF electric conductivity.[8,9] Also the fabrication of electrodes, usually made by a deposition of slurry of the synthesized powder, requires a long time of preparation and a large amount of precursor materials and MOFs, particularly if a second pyrolysis process is performed. However, particular properties of MOFs like their stable porous structure that can promote mass transport,[10] high tolerance to the change of volume during charge/discharge,[11] the redox activity of the metal node and/or organic linker,[12,13] and their hydrophobic nature can improve the cycle life and safety of batteries and can enable them to advance beyond lithium ion battery technology.

One such technology is the lithium metal battery, in which the anode is made of lithium metal. In this type of battery, the

[a]*Instituto de Nanociencia y Materiales de Aragón (INMA), CSIC-Universidad de Zaragoza, Zaragoza, 50009, Spain. E-mail: mharo@unizar.es*
[b]*Departamento de Química Física, Facultad de Ciencias, Universidad de Zaragoza, Plaza San Francisco, Zaragoza, 50009, Spain*
[c]*Departamento de Ciencia y Tecnología de Materiales y Fluidos, EINA, Universidad de Zaragoza, Zaragoza, 50018, Spain*

† Electronic supplementary information (ESI) available. See DOI: https://doi.org/10.1039/d3dt00876b

anode is no longer a lithium-ion host material but the lithium metal, which allows the energy and power density as well as the maximum theoretical open-circuit voltage to be increased.[14] For this technology, the suppression of lithium dendrites is necessary, using an optimized solid electrolyte or a protective layer on the top of lithium.[15,16] A further advancement is the anode-less battery, in which the Li^+ ions from the cathode and electrolyte are reduced to the Li metal directly on the anodic collector forming the "anode".[17] These anode-free batteries increase both the gravimetric and volumetric energy density, while improving safety, since no extra metallic lithium is included in the cell. However, anode-less batteries have the same concern of lithium dendrite growth, and thus protective layers are also required. Protective layers should be electrochemically and mechanically stable and homogeneous to avoid the formation of preferential channels or lithium depletion areas, which facilitate dendritic lithium deposition.[18,19] In this context, MOFs can be great candidates to fulfill all the requirements due to their ordered porosity and synthetic versatility.[17,20,21]

Among the different MOF families, 2D MOFs based on triphenylene[22] are promising materials for batteries due to their high electric conductivity caused by the presence of π delocalized electrons in the planar structure and by π–π stacking out-of-plane.[23] Although the fabrication of extended uniform 2D-MOF thin films is still challenging, in recent years there has been relevant progress in the creation of MOF nanosheets utilizing the interfacial reaction between the organic ligands and the metal ions at the air–liquid or liquid–liquid interfaces.[22,24,25] According to these studies, after a certain lapse of time the 2D MOF film is spontaneously formed at the air–liquid interface. The Langmuir technique is based on the formation of monolayers at the air–liquid interface and allows the area per molecule to be controlled by a mechanical compression process while measuring the surface pressure. Next, transfer of the monolayers from the air–liquid interface to a solid substrate can be performed at a controlled surface pressure to maintain a similar film structure throughout the deposition cycles. This bottom-up synthesis technique allows high control of the structure and requires a minimum amount of precursor materials.

To the best of our knowledge, the Langmuir technique is used here for the first time as the synthesis procedure of a MOF to study its electrochemical response in a lithium battery. In particular, the MOF studied is nickel 2,3,6,7,10,11-hexahydroxytriphenylene, $Ni_3(HHTP)_2$ (Fig. 1a). The optimization of the MOF film at the air–liquid interface includes a crystallization time step at a specific ligand surface density during the traditional compression process. *In situ* UV-vis reflection and synchrotron X-ray fluorescence and grazing-incidence diffraction measurements reveal that $Ni_3(HHTP)_2$ is spontaneously formed at the air–liquid interface, but crystalline domains can only be detected after the additional crystallization time, as opposed to a continuous barrier compression process. The transferred $Ni_3(HHTP)_2$ films are studied as working electrodes in coin cell Li half-cell batteries, without adding any additive (a binder and electron conductor carbon) and without using any other additional solvent (usually electrode slurries are formed with *N*-methyl pyrrolidone). The CV plots and XPS spectra before and after cycling reveal the oxidation of Ni from +II to +III during Li^+ intercalation while the negative charges are accumulated in the HHTP moieties. Despite the similarity of $Ni_3(HHTP)_2$ with analogous MOFs, such as $Co_3(HHTP)_2$ [26] and $Cu_3(HHTP)_2$,[27,28] the metal node exhibits different redox behavior during lithiation processes. Finally, galvanostatic plating–stripping cycles are performed using as working electrodes bare copper and copper covered with $Ni_3(HHTP)_2$. In the latter case, the incorporation of crystallization time is the determining factor in enhancing the coulombic efficiency of the $Ni_3(HHTP)_2$ covered copper, especially in the first cycles revealing that it can act as a protective layer on the top of the battery anode. Beyond being a useful tool to screen MOF-materials, the Langmuir technique can be coupled to roll-to-roll technology, which will allow the fabrication of large dimensions of protective layers on the top of flexible substrates.[29]

2. Experimental

2.1. MOF film synthesis and characterization

$Ni_3(HHTP)_2$ was *in situ* synthesized at the air–liquid interface using a Langmuir Teflon trough (NIMA, Model 720) with a symmetrical double-barrier configuration and dimensions of 720 × 100 mm^2. 1 mg of 2, 3, 6, 7, 10, 11-hexahydroxytriphenylene (HHTP, TCI > 95.0%) was first dissolved in 20.0 mL of methanol (POCH Basic, 99.8%) and then 80.0 mL of chloroform (Fluka ≥ 99.5%) was added under continuous stirring, for a final concentration of 0.01 mg mL^{-1}. HHTP solution was spread on the aqueous subphase containing 5 mM of nickel acetate ($Ni(Ac)_2$) (Sigma-Aldrich, ReagentPlus ≥ 99.0%) and 10 mM of sodium acetate (NaAc) (Sigma-Aldrich, ReagentPlus ≥ 99.0%) dissolved in ultrapure Milli-Q water in the Langmuir trough. This device registers the surface pressure *vs.* area (π–*A*) isotherms at 20 ± 1 °C during barrier compression movement using a Wilhelmy balance with a filter paper plate. Surface potential measurements were performed with a KSV Nima Spot Surface Potential Sensor. Brewster angle microscopy (BAM) images were recorded with a KSV Nima Micro BAM using a red laser (50 mW, 659 nm) as a light source with a fixed incidence angle of 53.1° and with a spatial resolution of the optical system of 6 mm per pixel. UV-vis reflection spectra were registered with a Nanofilm Technologie GmbH reflection spectrometer. Grazing-incidence X-ray diffraction (GIXD) *in situ* measurements at the air–liquid interface were performed at the SIRIUS beamline of Synchrotron SOLEIL (Saint Aubin, France), using an incident X-ray beam of 8 keV (λ = 0.155 nm), a beam size of 0.1 × 2.0 mm^2 ($V \times H$), and an incidence angle of 2.0 mrad with the aqueous surface below the total external reflection critical angle value of the air–liquid interface (2.7 mrad at 8 keV). The detection set-up consisting of a 2D PILATUS2 (Dectris, Switzerland) detector combined

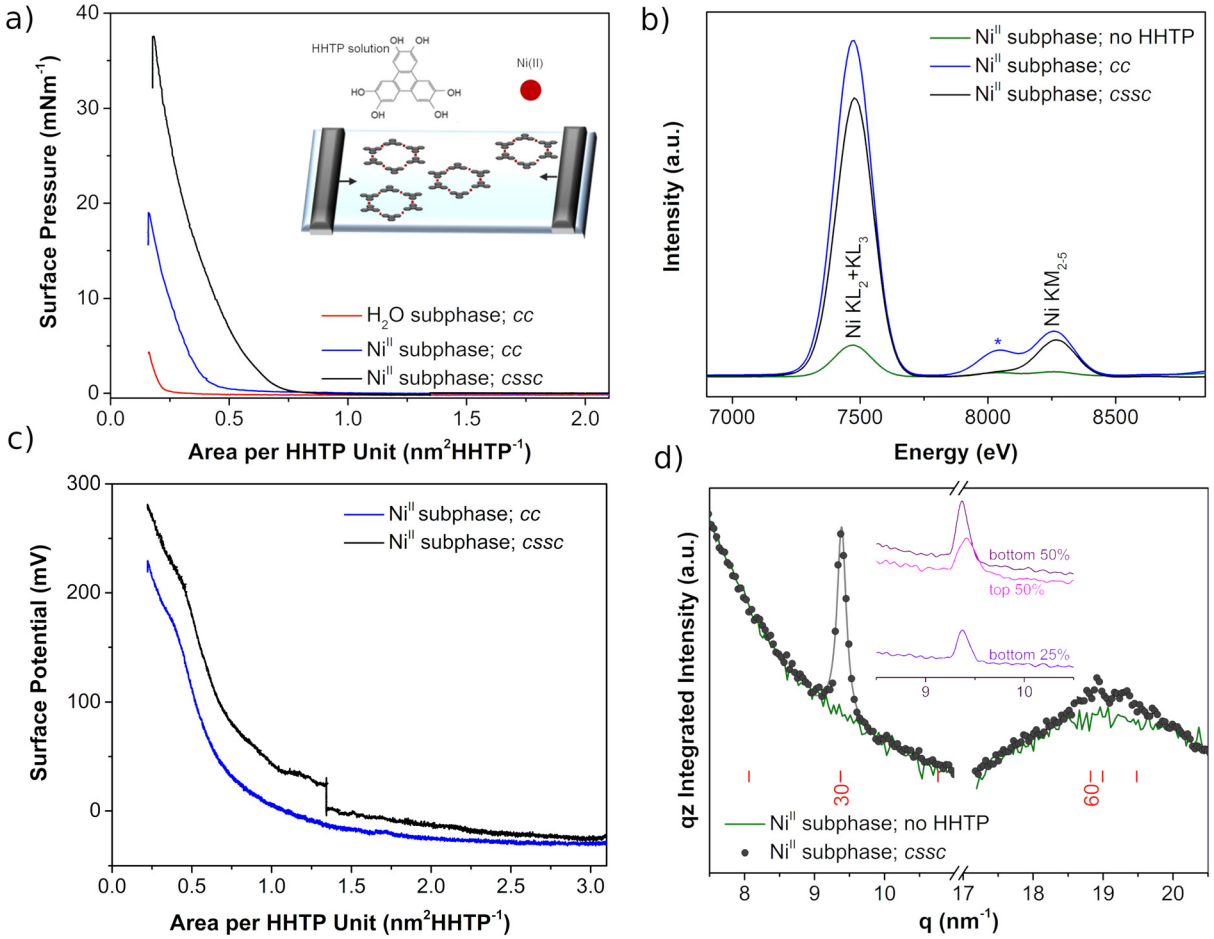

Fig. 1 (a) Surface pressure (π) *vs.* area per HHTP unit isotherms of the Langmuir films of HHTP on the water subphase (red), and HHTP on the Ni^{II} subphase following the cc (blue) and cssc (black) compression protocols. Inset: scheme of the HHTP molecule and of the Langmuir film when the subphase contains Ni^{II}. Although the compression process starts at 3.2 nm^2 $HHTP^{-1}$, the isotherms are represented from 2.1 nm^2 $HHTP^{-1}$ to show clearly the differences in including the cation in the subphase and the compression protocol. (b) Portions of the X-ray fluorescence spectra of the films formed by HHTP over the Ni^{II} aqueous subphase at 1.3 nm^2 $HHTP^{-1}$ (cc protocol, the blue line) and after 3 hours at 1.3 nm^2 $HHTP^{-1}$ (cssc protocol, the black line). The spectra of the Ni^{II} subphase are shown as a full green line. The grey star indicates the detection of Cu which is present at variable intensities in all spectra due to Cu in the experimental set-up. (c) Surface voltage (ΔV) *vs.* area per HHTP unit isotherms of the Langmuir films of HHTP on the Ni(II) subphase following the cc (blue) and cssc (black) compression protocols. (d) Raw *in situ* GIXD data for the Ni(II) subphase (the green line) and for the film formed by HHTP over the Ni(II) aqueous subphase after 3 hours at a constant area = 1.3 nm^2 $HHTP^{-1}$ (cssc protocol, black symbols). Red ticks indicate the calculated positions of the peaks for a 2D structural model of the $Ni_3(HHTP)_2$ planes. The full grey line shows a Lorentzian fit of the [30] reflection yielding q = 9.387 nm^{-1}. Inset: cssc protocol GIXD data for the different portions of the detectors as indicated, showing the absence of modulation along q_z and therefore pointing at a pure 2D film.

with a Soller collimator of 0.05 degree resolution was continuously scanned over the in-plane 2θ angle in order to record the horizontal and vertical intensity distributions. Peak adjustment was performed with the Q_z-integrated intensity. Total reflection X-ray fluorescence (TRXF) measurements were performed simultaneously with GIXD with a one element silicon drift detector (XFlash 430 M, Brüker, Germany) equipped with a collimator and mounted at 30° with respect to the vertical direction towards the X-ray source in order to reduce the elastic peak that would otherwise saturate the detector. Monolayers were prepared in a dedicated Langmuir trough enclosed in a gas-tight chamber flushed by a water saturated Helium gas flow to reduce gas scattering and to avoid the damage of the monolayer by the beam. Temperature was kept constant thanks to a water circulating bath at 20 ± 1 °C.

Langmuir–Schaeffer (LS) films were fabricated in a Teflon KSV-NIMA trough, model KN 2003 of dimensions 580 × 145 mm^2. Different substrates were used in the function of the characterization technique. The Quartz crystal was the substrate for UV-vis characterization with a Varian Cary 50 Bio spectrophotometer. Mica was selected for atomic force microscopy (AFM) characterization. AFM images were obtained with a commercial instrument (Multimode 5 Nanoscope 7.3, Veeco) operated in tapping mode. Measurements were carried out under ambient conditions with NSC15/AlBS silicon cantilevers (MikroMasch) at a 325 kHz nominal resonance frequency.

MOF mass deposited onto QCM substrates (5 MHz ATcut QCM crystals from Stanford Research Systems) was determined using a Stanford Research Systems (SRS) QCM200 system equipped with a QCM25 crystal oscillator working at 5 MHz. QCM crystals were placed in a O100RH Kynar crystal holder before and after each film transfer, and the mass increases were calculated from frequency changes using the Sauerbrey equation, $\Delta f = -C_f \Delta m$, where Δf is the observed frequency change, in Hz, C_f is the sensitivity factor of the QCM crystal provided by the manufacturer (0.0566 Hz cm^2 ng^{-1}), and Δm is the change in mass per unit area.

2.2. MOF tests in Li semi-batteries

The substrate to deposit the MOF was Cu foil (Alfa-Aesar >99.9%). After MOF film deposition, the samples were dried during 12 h at 60 °C under vacuum and cut into discs of 8 mm in diameter (the electrode and separator disc cutting machine, TOB). These discs were saved in an Ar glovebox and used as electrodes in Li-ion batteries assembled in a half-cell configuration, in which Li foil (Sigma-Aldrich, thickness 1.5 mm) was used as the counter and reference electrodes. The electrolyte was 1 M $LiPF_6$ ethylene : diethylene carbonate (EC : DEC 1 : 1, Sigma-Aldrich) embedded in a glass microfiber (Whatmann GF/C™). The Li-ion half-cell battery was crimped in a CR2032 coin cell with a hydraulic manual crimper (TMAX-JK-KF20-TC).

A M204 Autolab Methrom potentiostat/galvanostat was used for galvanostatic and cyclic voltammetry characterization. Galvanostatic plating/stripping cycles were performed at 0.15 mA cm^{-2} during 2 hours with cut-off limits of +0.6 V and −0.6 V *vs.* Li/Li$^+$, except the first plating that was performed at 0.05 mAcm^{-2} for 6 hours to facilitate the formation of a more stable solid electrolyte interface (SEI).

Pristine and cycled electrodes were characterized by X-ray photoelectron spectroscopy (XPS) using an AXIS SupraTM ultra DLD spectrometer from Kratos equipped with a monochromatic Al (Kα) X-ray source (1486.6 eV) using a pass energy of 20 eV. The photoelectron take-off angle was 90° with respect to the sample plane. The XPS binding energies reported in this work were referenced to the maximum of the C 1s peak at 284.6 eV.[30] After battery cycling, the reference applied was the same and the analysis was qualitative since the SEI was not fully removed from the top of the sample. The data treatment was performed using the CasaXPS software. For this study, a Swagelok cell was used to open it inside the glovebox after battery cycling and the samples were cleaned with ethylene carbonate.

3. Results and characterization

3.1. Synthesis of $Ni_3(HHTP)_3$ layers at the air–liquid interface and on solid substrates by the Langmuir–Schaeffer (LS) technique and transference process

Langmuir $Ni_3(HHTP)_2$ films were synthesized by dropping the HHTP solution over the aqueous solution containing Ni^{II} as a subphase in a Langmuir trough. Next, the compression process proceeds following two different protocols: (i) typical constant compression (cc) in which the compression of the barriers is constant at 10 cm^2 min^{-1}, and (ii) compression + crystallization step + compression (cssc) in which the compression of the barriers is first done at 10 cm^2 min^{-1} from 3.2 nm^2 HHTP^{-1} to 1.3 nm^2 HHTP^{-1}, then stopped for 3 hours at this constant area, and finally continued further at 10 cm^2 min^{-1} until collapse of the film.

The surface pressure-area isotherms (π–*A*), Fig. 1a, show that the Ni^{II} cations present in the subphase produce more expanded isotherms than those when the subphase is water, suggesting the incorporation of the cations at the interface. This is confirmed by the X-ray fluorescence spectra at the air–water interface (Fig. 1b). The KL and KM bands of Ni at 7460 and 8260 eV increase dramatically when the HHTP molecules are dispersed on the Ni^{II} subphase, and the intensity hardly varies during the compression process regardless of the protocol followed. Then, interfacial coordination reactions between the building molecular units of the air–liquid interface and the metal ions of the subphase are initiated spontaneously after dispersion of the organic ligand onto the subphase, in good agreement with the literature.[31] However, the compression protocol affects the π–*A* isotherm plots (Fig. 1a), with the film being more expanded for the cssc protocol, which also shows higher collapse pressure. This is likely due to the inclusion of the crystallization step which shows an increase in the structural order distance, producing crystals with larger lateral domains. Another subtle observation is the decay of surface pressure with time when barriers are stopped in the cssc protocol (Fig. SI.1†), which can be fitted to an exponential equation of type $\pi = \pi_0 \exp(-t/t_1)$.[32] The obtained value for t_1 is ~10 600 s, which is in the order of those reported for the rearrangement of nanoparticles[33] and liquid crystal polymers[34] at the air–liquid interface, and an order of magnitude larger than the surface fluctuation damping when the barriers change from mechanical compression to a steady state.

The effect of adding crystallization time during the compression process is observed in the surface potential values, ΔV, of the film. Fig. 1c shows similar ΔV isotherms from the initial value of the compression up to 1.3 nm^2 HHTP^{-1}. Next, an increase of ~50 mV occurs when the barriers stop at 1.3 nm^2 HHTP^{-1} in the cssc protocol, and again the same shape is observed between 1.3 nm^2 and the final value of the compression, but showing a difference of ~50 mV. The gain in ΔV has been previously associated with an increase of ordered domains as in polymer films,[35] with the incorporation of water molecules into the Langmuir film,[36] or with an increase in the contribution of the double layer, ψ^0.[37] In the current study, the ΔV increase with time also follows first order kinetics, $\Delta V = \Delta V_0 \exp(t/t'_1)$ (Fig. SI.2†), similar to the decay observed for π, suggesting that domain upregulation and rearrangement are the most plausible phenomena. This is in good concordance with *in situ* grazing incidence synchrotron X-ray diffraction (GIXD). Detectable diffraction is only observed in the later stages of the 3 h crystallization time in the cssc protocol (Fig. 1d). A relatively intense diffraction peak appears at

approximately q = 9.4 nm^{-1}, corresponding to a Bragg bar, with intensity at all q_z (the inset in Fig. 1d), demonstrating the 2D character of the objects giving rise to the diffraction. In addition, weaker diffraction is observed at *ca.* 19 nm^{-1}, with intensity also detectable at all q_z. Both GIXD peaks can reasonably be attributed to the [30] and [60] reflections of a structural model based on the $Ni_3(HHTP)_2$ structure (Fig. SI.3†), but without intercalated hydrated molecules.[38] Therefore, the crystallization step aids the formation of (larger) crystalline domains with respect to the typical cc compression protocol, and these crystalline domains coalesce together upon compression.

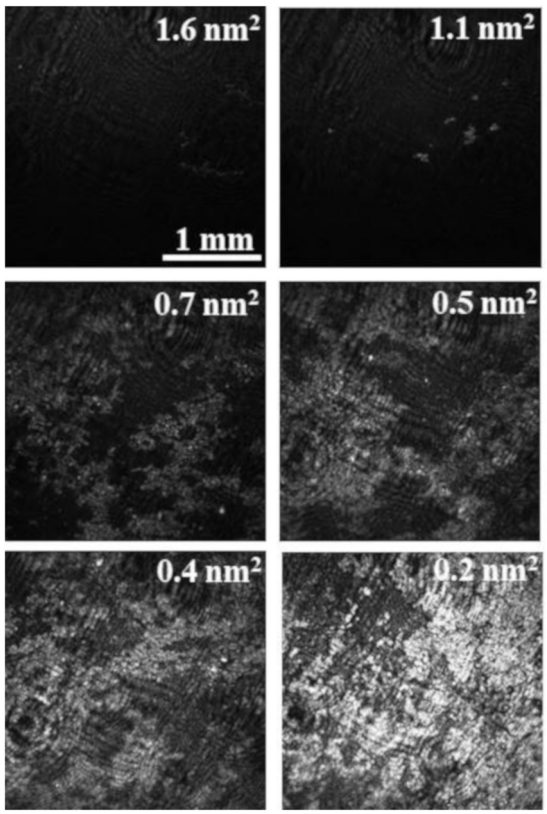

Fig. 2 BAM images of the Langmuir film of $Ni_3(HHTP)_2$ at different areas per HHTP during the cssc compression process.

The BAM images (Fig. 2), recorded in the cssc compression process, show the formation of domains of a few micrometers at larger areas (1.1 nm^2 HHTP^{-1}). These domains coalesce with decreasing surface area, forming worm-like domains and empty spaces at 0.7 nm^2 HHTP^{-1} where π starts to increase. Upon further compression, lighter gray spots begin to appear indicating the regions of increased thickness, while dark areas (no molecular coating or very thin layer) are still observed at 0.5 nm^2 HHTP^{-1}. At 0.4 nm^2 HHTP^{-1}, worm-like domains are observed similar to those at 0.7 nm^2 HHTP^{-1} but brighter. These images suggest that the Langmuir film consists of regions formed by multilayer domains over thinner or bare areas, rather than an appropriate monomolecular film at the air–water interface. A second brightness increase in the BAM images appears at 0.2 nm^2 HHTP^{-1}, where the π–A isotherm shows film collapse.

The UV-vis reflection (ΔR) spectra of $Ni_3(HHTP)_2$ at the air–liquid interface during the cssc compression process (Fig. 3a) show the characteristic strong absorption in the UV and blue visible regions (below ~450 nm) corresponding to the π–π^* transition of the catecholate linking moieties.[25,39] The second peak reported for the HHTP-based MOFs containing different metal nodes (Ni, Co and Cu) appears at 620 nm and is attributed to the ligand-to-metal charge transfer transition.[25,39] This peak shifts to longer wavelengths in the spectra of the MOF formed at the air–liquid interface due to the highly polar environment in the presence of the aqueous subphase.[40] However, the UV-vis reflection spectrum of the Langmuir film

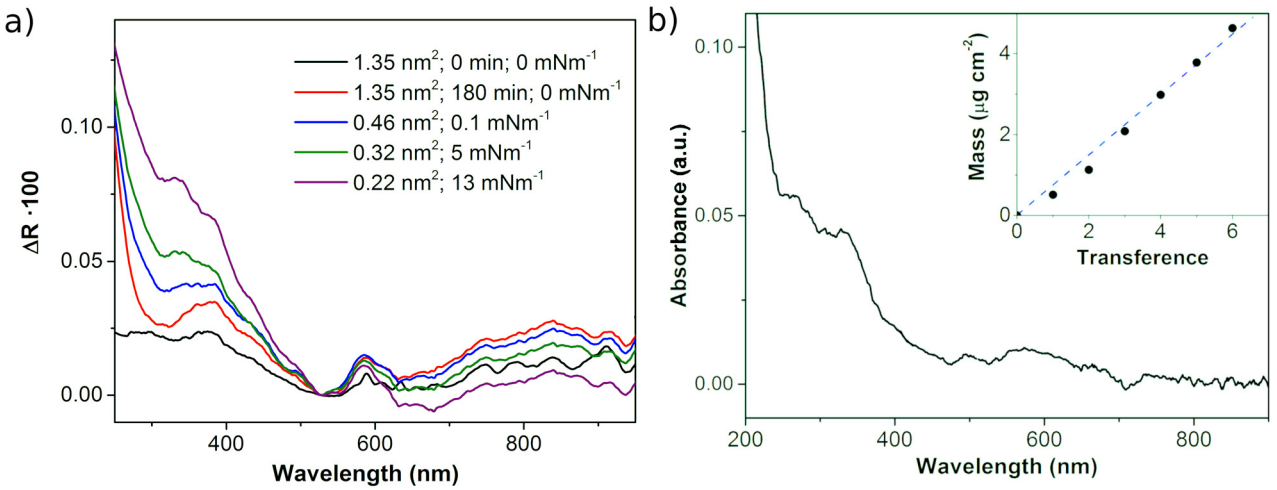

Fig. 3 (a) Reflection UV-vis spectra of $Ni_3(HHTP)_2$ Langmuir films at different areas per HHTP during the compression process with the cssc protocol. (b) UV-vis absorption spectrum of the $Ni_3(HHTP)_2$ LS film (4 transferences) transferred at 10 mN m^{-1}. Inset: Mass density increase of the LS film with the number of transference cycles at 10 mN m^{-1}.

formed with the cc protocol differs significantly from this description (Fig. SI.4†), probably due to the formation of smaller light-scattering domains. The characteristic UV-vis spectrum of $Ni_3(HHTP)_2$ with the broad band of charge transfer at ~600 nm is observed in the transferred film (Fig. 3b), once the polar aqueous subphase is not present. This observation suggests that the film formed at the air–liquid interface, which consists of $Ni_3(HHTP)_2$ crystalline domains, can be transferred to a solid substrate without any appreciable change in the film. In addition, the mass of the films after several transfers was weighed with a QCM showing a linear increase in mass with the number of cycles, passing through the origin. This linear mass increase indicates that the films transferred from the air–liquid interface to the substrate are homogeneous when π is maintained at 10 mN m^{-1} even though the films are formed by coalescing crystalline domains. The XPS spectra of the LS film formed on the Cu substrate (Fig. 7) show the characteristic $Ni_3(HHTP)_2$ peaks,[41–43] confirming that extended $Ni_3(HHTP)_2$ framework domains are formed. Further discussion is performed in the next section.

The LS films of 1, 3 and 5 transference cycles were analyzed by AFM microscopy (Fig. 4). A nearly full surface coverage composed of worm-like domains of about 1.5 nm height is already observed after 1 transference cycle. This height is larger than a monolayer thickness (~ 3.3 Å)[44] and suggests the formation of domains with 3–4 molecular $Ni_3(HHTP)_2$ planes lying parallel to the surface. The worm-like structures are of a few nanometers in thickness and form larger circular domains of a few micrometers, in good agreement with the film described at the air–liquid interface. This structure is similar to other LS films of MOFs.[45] Despite the worm-like fine structure, a full surface coverage is obtained after 3 transference cycles. In the film of 5 transferences, the worm-like fine structure is less clearly observed, and new round domains of ~5 nm appear.

3.2. Study of the electrochemical response of $Ni_3(HHTP)_2$ layers against Li metal

The preparation of $Ni_3(HHTP)_2$ electrodes was carried out directly on a Cu foil substrate without the addition of any binder or electronic conductor, performing 20 transference cycles. Fig. 5 shows the AFM images of these electrodes. The images show a complete coating of the substrate with small defects and round domains with a diameter in the range of 100–200 nm and 2–6 nm in height. This type of rounded

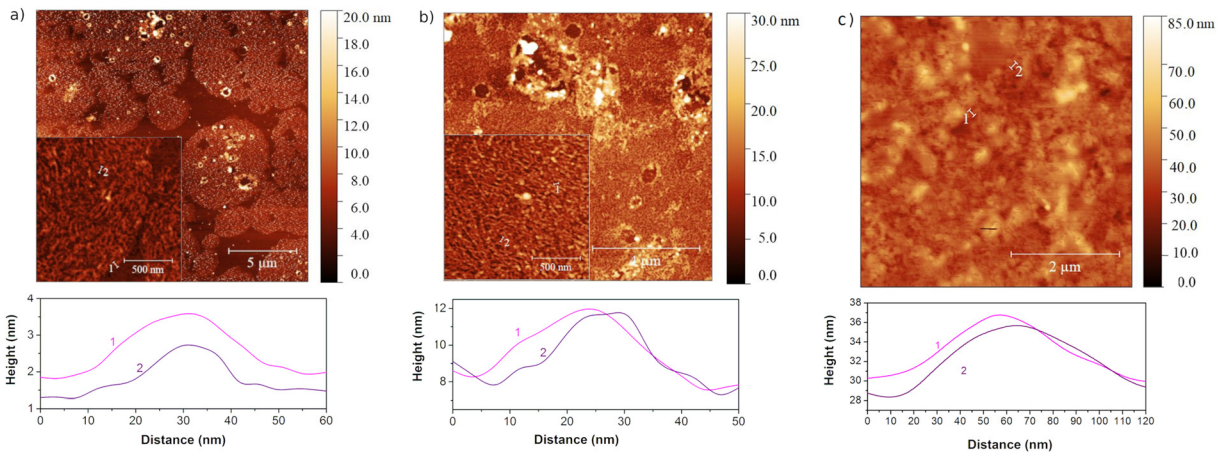

Fig. 4 AFM images and representative height profiles for $Ni_3(HHTP)_2$ LS films with: (a) 1, (b) 3, and (c) 5 transferences from Langmuir films at 10 mN m^{-1} formed with the cssc protocol.

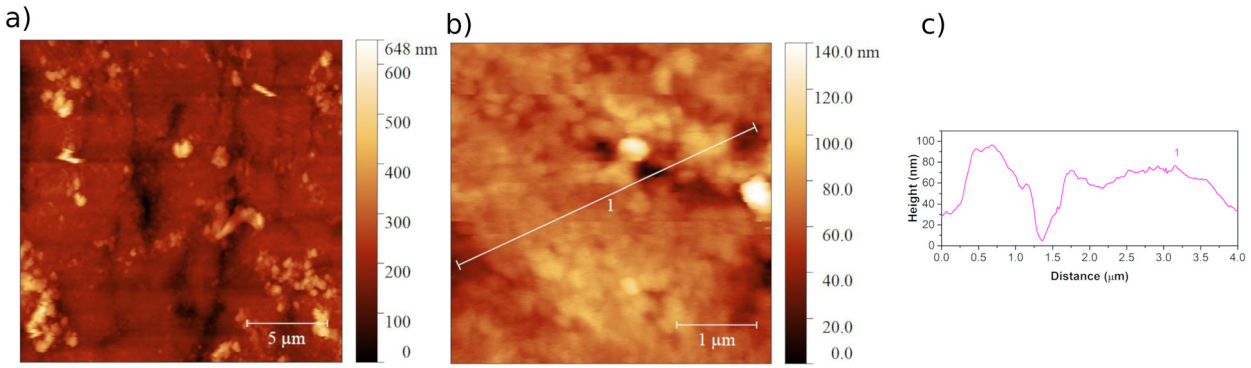

Fig. 5 (a) and (b) AFM images of the $Ni_3(HHTP)_2$ electrodes (20 transferences) on Cu foil and (c) the corresponding height profile.

domain was already observed in the 5-transfer samples (Fig. 4c), which reveals that this organization is the most prevalent after 5 transfers. While, the worm-like structure observed in 1 and 3 transferences cannot be observed with clarity, probably because of the roughness of the surface. In this case, the Cu substrate contributes to both the roughness of the sample and the presence of defects, which can have a height of ~100 nm. The roughness and the presence of steps on the Cu surface are observed on bare copper (Fig. SI.5†), and are in agreement with the literature.[46]

The electrochemical response of the $Ni_3(HHTP)_2$ film with lithium was recorded in an assembled coin cell. Fig. 6a shows the CVs of the half-cell batteries when the working electrode is a $Ni_3(HHTP)_2$ LS film (20 transferences, cssc protocol) on copper foil and when it is bare copper. In the case of bare Cu, the oxidation of Cu is observed above 3 V *vs.* Li/Li^+ which returns in a loop in the cathodic direction that can be ascribed to the oxidation of the substrate and its posterior solution. This effect is efficiently avoided when the LS film covers the Cu film. In the case of the LS film, the 3 CV cycles match indicating the good reversibility of the electrochemical processes, with two broad reduction/oxidation peaks centered at ~1.4 V and ~0.5 V *vs.* Li/Li^+ in the cathodic sweep and their respective anodic peaks at ~2.0 V and ~1.2 V. The broad peaks suggest a gradual multipass insertion of Li^+, stabilized with the reduction of the O atoms in the organic ligands[47] and by electrostatic interaction with the π-electron cloud of the phenyl rings.[48] This behavior obeys a pseudocapacitive mechanism described for MOFs in Li batteries,[49–51] in which both redox and electrostatic mechanisms are involved. Both contributions can be differentiated from the power law relation $i = av^b$, where i is the measured current and v is the sweep speed at which the CVs are obtained (Fig. SI.6†). The slope of the $\log v$ *vs.* $\log i$ plot gives the b parameter, which has a value between $b = 0.5$ for the diffusion–dominant process (related to faradaic processes) and $b = 1$ for the completely capacitive effect (related to double layer capacitance).[52] Here the b-value in the range of 0.5–2 V is between 0.72 and 0.85 (Fig. SI.7†), which confirms the pseudocapacitive mechanism. Fig. 6b shows the capacitive contribution in the CV obtained at 0.5 mV s^{-1}, which represents a 33% contribution. After the CV cycles at different sweep rates (0.1 mV s^{-1}, 0.5 mV s^{-1}, 1 mV s^{-1}, 5 mV s^{-1}, 10 mV s^{-1}, and 50 mV s^{-1}), other 3 cycles were performed at 0.1 mV s^{-1} showing high reproducibility in the shape of the plot at the beginning and at the end of the measurement (Fig. SI.8†). This result indicates that no significant degradation process occurs in the MOF during battery cycling.

The XPS spectra of the electrodes before and after being cycled in a Li half-battery at 0.1 V *vs.* Li/Li^+ provide information on changes in the oxidation state or chemical environment of the $Ni_3(HHTP)_2$ components. The high resolution Ni 2p spectrum before cycling (Fig. 7a) shows two sets of peaks at 856.2 and 873.8 eV with their respective satellites, which correspond to the $2p_{3/2}$ and $2p_{1/2}$ levels, respectively, of the emission lines of Ni^{II}. Also, the 3p peaks of Ni^{II} are observed at 68.6 eV and 76.5 eV (Fig. 7b). These spectra prove that only one type of Ni^{II} is present within the LS film when it is deposited.[41] The 2p peaks attributed to Ni^{II} are significantly reduced in the cycled sample, where two new peaks appear at 858.1 eV and 876.8 eV related to $2p_{3/2}$ and $2p_{1/2}$ of Ni^{III}. The same behavior is observed in the high resolution spectrum of Ni 3p, a region in which the 1s Li^I band appears for the cycled sample. Therefore, the intercalation of Li ions in the MOF presumably induces the oxidation of Ni^{II} to Ni^{III} for the most part. The high resolution C1s and O1s XPS spectra (Fig. SI.9†) show the presence of traces of the SEI in the cycled samples; so it is not possible to perform a quantitative analysis. Qualitatively, the characteristic C1s and O1s bands described for the triphenylene-based MOFs are observed in the uncycled samples.[42] Upon cycling, the bands become narrow indicating a preferential chemical environment of C and O, most likely due to a

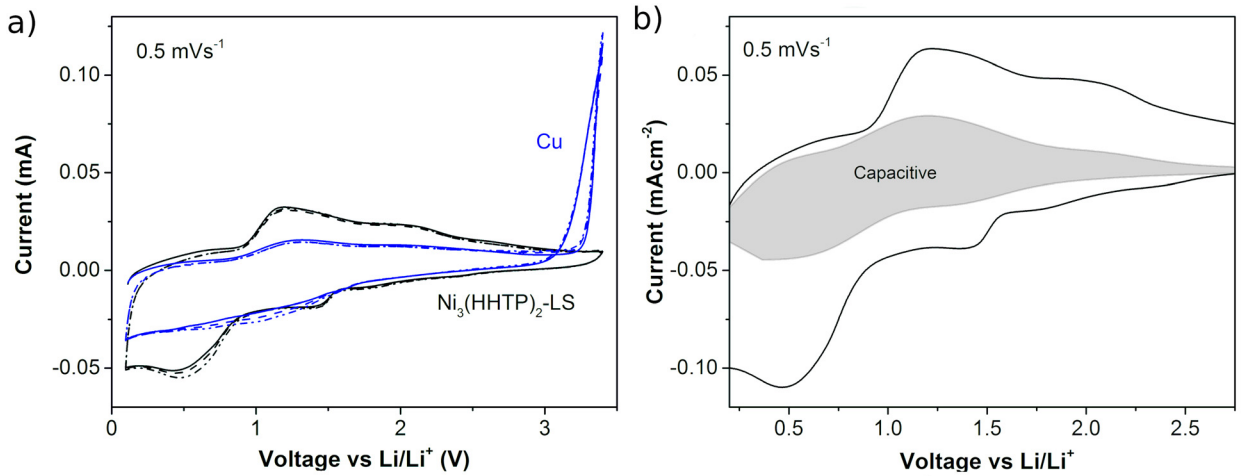

Fig. 6 (a) 3 CV cycles of a Li half-cell battery using bare Cu foil or Cu foil covered with a LS film of 20 transferences of $Ni_3(HHTP)_2$ at 0.5 mV s^{-1}. (b) Percentage of capacitive response within the CV registered at 0.5 mV s^{-1}.

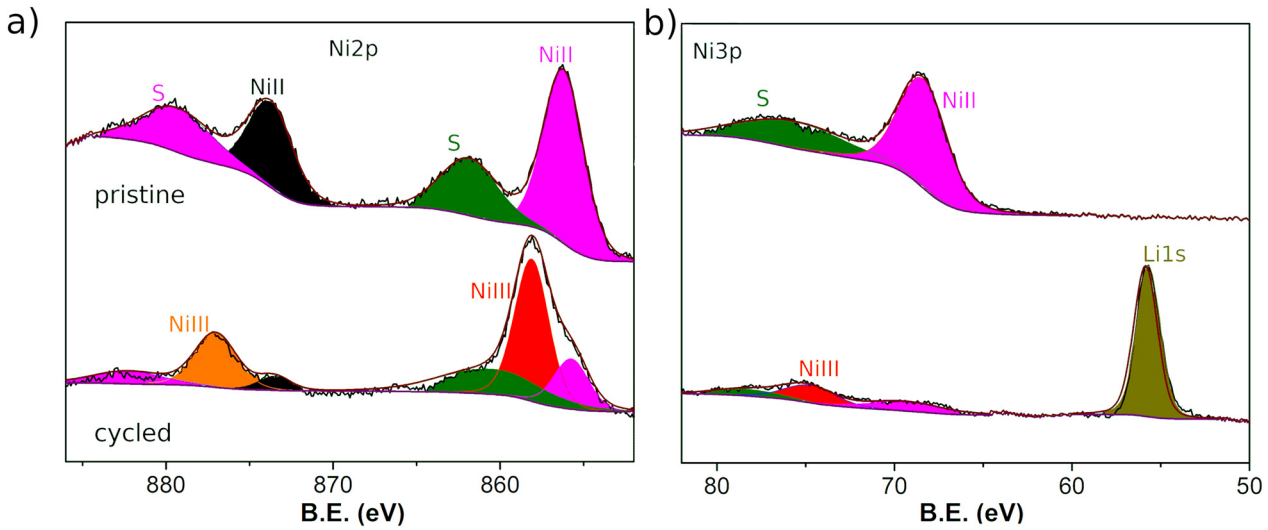

Fig. 7 High resolution XPS spectra of: (a) Ni 2p, and (b) Ni3p and Li1s for the pristine $Ni_3(HHTP)_2$ LS film (top) and after being cycled as electrodes in a half-cell battery dissembled when the voltage was 0.1 V *vs.* Li/Li^+ (bottom).

catecholate configuration[53] that accumulates the negative charge upon cycling at 0.1 V *vs.* Li/Li^+.

Altogether, the XPS data suggest Ni oxidation that may stabilize the negative charge accumulation on the ligand, and may also explain the protection of the Cu foil from being oxidized, as observed in Fig. 6a. Taking all this into account, the electrochemical process we propose is:

$$Ni_3^{II}(HHTP)_2^{-III} + 3e^- + 3Li^+ \rightarrow Li_3^{I}Ni_3^{III}(HHTP)_2^{-VI} \quad (1)$$

This electrochemical behavior described for the $Ni_3(HHTP)_2$ film differs from those described for $Cu_3(HHTP)_2$ and $Co_3(HHTP)_2$ MOFs cyclized in Li batteries. In the former case, Cu is reduced from Cu^{II} to Cu^{I}, while in the latter Co^{II} does not change its oxidation state.[26–28] Thus, in principle, metal oxidation reduces the faradaic capacity of $Ni_3(HHTP)_2$ compared to those of other triphenylene-based MOFs. In particular, the study of the $Co_2(HHTP)_3$ MOF[26] reported a capacity of 332 mA h g^{-1} at 0.1 A g^{-1} *vs.* the value of 631 mA h g^{-1} at 0.2 A g^{-1} for $Cu_2(HHTP)_3$.[27] However, it should be noted that the final organization of the MOFs in the electrodes determines the final capacity, being less than 100 mA h g^{-1} at 1C for $Cu_2(HHTP)_3$.[28] Particularly, in the case of $Ni_3(HHTP)_2$, the capacitive contribution is significant, which could be favored and stabilized by the higher negative charge on the organic part. Noticeably, an important difference in our sample from these reported studies is the thickness of the films, being an order of magnitude smaller in the current study; so the effect of the film thickness cannot be completely discarded in terms of electrolyte embedding within the MOF that can facilitate Ni oxidation or even the depth of the XPS analysis.

The potential of the $Ni_3(HHTP)_2$ LS film as a protective layer for various Li half-cell batteries has been studied with the working electrodes: pristine copper (Cu) foil and LS films fabricated with the cssc protocol (20 transferences) and cc protocol (20 transferences). Fig. 8a shows the first galvanostatic cycles of plating and stripping for the three semi-batteries. During the Li plating process the Li^+ ions from the electrolyte diffuse through the ultrathin MOF layer and are reduced to Li metal at the top of the Cu collector. Theoretically, the reduction should occur at 0 V *vs.* the Li/Li^+ reference, but it occurs at a lower voltage which is the nucleation overpotential (μ_{nuc}); so the peak indicates the onset of Li deposition.[54] Next, the plating process is controlled by mass transfer diffusion of Li^+ ions through the deposited layer, which determines the plateau potential (μ_{pla}).[54] The first plating plot (at a lower current density to facilitate the formation of a more stable SEI) is very similar for the three semi-batteries with a μ_{pla} value of ~−13 mV and a μ_{nuc} value between −20 mV and −27 mV. After this first cycle, the plating plot obtained at a higher current density shows higher μ_{nuc} and μ_{pla} values due to the kinetic effect. In the case of the cssc sample, the plating plots are square in shape and with high reproducibility throughout the first eleven cycles, although μ_{pla} increases slightly after the 9th cycle. The two batteries fabricated with cc and Cu working electrodes show similar behavior. In these samples, μ_{pla} is slightly larger than that in the cssc sample and the plating plot loses the square shape: at the 10th cycle it increases with time instead of decreasing, and after the 11th cycle it first increases and then decreases. The fact that the plating does not occur in a plateau points that other effects besides the Li^+ diffusion control the process, probably kinetic limitations or the formation of channels. This effect is not observed for the cssc sample (Fig. 8b), although an increase of overpotentials occurs during the first cycles, followed by cycles that show high reproducibility. On the other hand, the value of μ_{nuc} is similar in the three semi-batteries. These results suggest that the $Ni_3(HHTP)_2$ LS layer deposited using the cssc protocol aids to the diffusion of Li^+ ions to the Cu substrate, but does not produce any significant effect on the reduction of the nuclea-

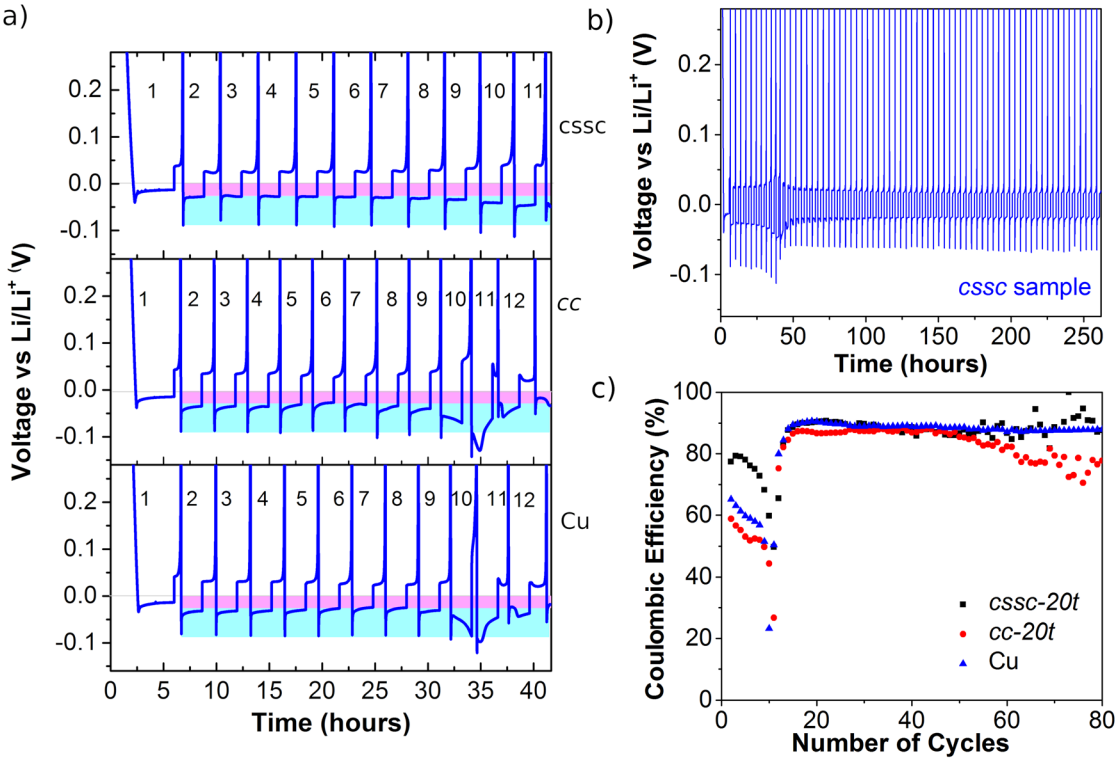

Fig. 8 (a) Plating–stripping galvanostatic plots for the half-cell batteries fabricated with the working electrodes: $Ni_3(HHTP)_2$ LS film fabricated with the cssc and cc protocols on Cu foil, and bare Cu foil. For ease of comparison, the μ_{pla} (~−28 mV) and μ_{nuc} (~−55 mV) points of the second cycle are shaded in pink and blue for the cssc sample (elongated for the other cycles), and the same shading dimensions are superimposed on the plots obtained for the cc and Cu semi-batteries. (b) Plating–stripping galvanostatic plots for the cssc sample half-cell battery along 80 plating–striping cycles. (c) Coulombic efficiency (CE) of Li^+ plating/stripping processes along 80 cycles.

tion overpotential. However, when the $Ni_3(HHTP)_2$ LS layer is fabricated with the cc protocol, the positive effect of Li^+ diffusion is not observed compared to the bare Cu substrate.

After the coating process, the stripping process begins at a positive voltage plateau. At the end of the ordered process, a rapid increase in the voltage is observed, due to an increase in the resistance associated with contact loss and the change in the open circuit voltage as the original $Ni_3(HHTP)_2$/Li cell is modified. Coulombic efficiency (CE) can be, then, calculated as a quantifiable indicator for the reversibility of plating/stripping processes, in which the electrons from irreversible reactions are also considered according to eqn (2):[55]

$$CE = \frac{\text{Number of } e^- \text{ from stripping } Li^+ + \text{Number of } e^- \text{ from electrochemical reactions}}{\text{Number of } e^- \text{ from depositing } Li^+ + \text{Number of } e^- \text{ from electrochemical reactions}} \quad (2)$$

The calculated CE values (Fig. 8c) are lower and decrease in the first 15 cycles from ~80% to ~50% for the sample cssc and from ~60% to 20% for the Cu substrate and cc sample. The lower CE values are related to the occurrence of irreversible side reactions that take place during SEI formation, which may be prolonged during the first 20 cycles. However, the cssc sample is the one with a considerably higher CE value than the other two samples, indicating a lower electrolyte consumption in the secondary reactions probably because a more ordered and stable SEI layer is formed. After these preliminary cycles, the CE value increases to near 90% values for the cssc and Cu half-cell batteries and to somewhat lower values for the cc sample. This change in behavior can be attributed to the transition between two different regimes with Li^+ ion capacity loss:[56] the first being due to the formation of the SEI, and the second being due to the encapsulation of electronically isolated Li^0. This transition is favored by the fact that the fabricated half-cells provide an "unlimited" Li system because the counter electrode is a metallic Li foil and the working electrode (bare Cu or covered by a nanometer-thick film) is "flooded" with the electrolyte; so that, despite the increase in the system impedance due to SEI formation, the introduction of the electrolyte is still sufficient to prevent battery termination.[55] In this new regime, the first system to fail is the cc sample, indicating that in this case the presence of the $Ni_3(HHTP)_2$ LS film without large 2D crystalline domains introduces higher impedance than that obtained for the bare Cu foil. While, the presence of larger crystalline domains in the

cssc sample shows scattered CE values after 50 cycles, in the range between 89% and 95%, principally. Considering the two contributions to the CE values, eqn (2), the higher values are probably due to the release of electrons in the electrochemical processes in the $Ni_3(HHTP)_2$ film, electrochemically active (eqn (1)), in contact with the SEI, since if it was due to an increase in the reversibility of the delithiation process itself one would expect a more homogeneous trend instead of such scattered values. To sum up, the fabricated $Ni_3(HHTP)_2$ LS films are not very efficient as protective layers for batteries without the anode, although the efficiency improves significantly with the film order. This deficit is presumably due to the ultra-thin nature of the fabricated films which are of a few nanometers compared to those found in the literature which are in the order of micrometers.[20,57–59] However, the good response in the first plating-stripping cycles and the higher CE values observed for the $Ni_3(HHTP)_2$ LS film fabricated with the cssc protocol suggest that this film is promising as a protective layer in anodes to form a stable SEI facilitating the Li^+ diffusion.

4. Conclusions

This study describes the benefit of including an additional crystallization time to enhance the 2D $Ni_3(HHTP)_2$ crystalline domain formation during the compression process at the air–liquid interface. This simple modification of the Langmuir technique provides a new parameter to control (crystallization time) in the *in situ* formation of MOFs at the air–liquid interface, which can enhance the extension of 2D domains and facilitate the integration of ultrathin films in practical devices. The electrochemical study of the $Ni_3(HHTP)_2$ LS film in a Li half-cell battery shows the oxidation of the Ni metal node from +II to +III, which can stabilize the accumulation of negative charge in the organic ligand besides protecting the Cu collector from oxidation. Related to the plating–stripping study, the CE plot previews that the $Ni_3(HHTP)_2$ LS film fabricated with the cssc protocol can reduce the side reactions related to the SEI formation and facilitate the Li^+ diffusion through it, so it can be used as a protective layer of anodes. Despite the fact that under the current conditions it does not work properly as a protective layer to reduce/avoid the formation of lithium dendrites in anode-free batteries, the low amount of the material used and the thickness of the ultrathin film are two relevant properties that can be optimized by the Langmuir technique for the design of future protective layers for anode-less lithium or other metal batteries.

Beyond the results obtained, the fabrication of Langmuir films of triphenylene-based MOFs provides a means to customize advanced materials, both through the nature of the metal ion node, with the Ni-based MOF having a different redox electrochemical behavior from the Cu or Co analogues, and the growth of 2D domains at the air–liquid interface, controlled by both the area per ligand and the crystallization time.

Author contributions

M. H. conceived the idea, designed the experiments, wrote the initial version of the manuscript, and supervised the work. I. C.-R. fabricated the half-cell batteries and performed and analysed the electrochemical study (CV and platting-stripping galvanostatic measurements). I. T. performed and analysed the *in situ* synchroton fluorescence and GIXD measurements. L. C. performed the characterization of $Ni_3(HHTP)_2$ Langmuir films by BAM, surface potential analysis, and UV-vis reflection spectroscopy and fabricated the electrodes and the half-cell batteries. B. D. performed preliminary studies for the optimization of the synthesis of $Ni_3(HHTP)_2$ at the air–liquid interface. O. L. performed the QCM tests and prepared the samples for AFM measurements. A. U. performed and analyzed the AFM measurements. O. R. proposed the material, performed the *in situ* synchroton fluorescence and GIXD measurements, and discussed the XPS data. I. G. conceived the idea of the addition of the crsytallization step in the compression process, designed the experiments, and supervised the work. All authors contributed to editing the paper.

Conflicts of interest

There are no conflicts of interest to declare.

Acknowledgements

The authors acknowledge the DGA/fondos FEDER (construyendo Europa desde Aragón) for funding the research group Platon (E31_20R) and the project LMP71_21. This work was also funded by MCIN/AEI/10.13039/501100011033 and ERDF "A way of making Europe" (PID2019-108247RA-I00 and PID2019-105881RB-I00). M. H. acknowledges the funding support from MCIN/AEI/10.13039/501100011033 for the Ramón y Cajal fellowship (RYC-2018-025222-I). I. T. gratefully acknowledges her DGA PhD fellowship. The authors would like to acknowledge the use of Servicio General de Apoyo a la Investigación-SAI, Universidad de Zaragoza. The authors thank the synchrotron SOLEIL for beamtime provision under projects 20191874 and 20210275 and are grateful to Prof. M. Goldmann and Dr P. Fontaine for their support during experiments.

References

1 S. R. Batten, N. R. Champness, X.-M. Chen, J. Garcia-Martinez, S. Kitagawa, L. Öhrström, M. O'Keeffe, M. P. Suh and J. Reedijk, *Pure Appl. Chem.*, 2013, **85**, 1715–1724.
2 H. Li, M. Eddaoudi, M. O'Keeffe and O. M. Yaghi, *Nature*, 1999, **402**, 276–279.
3 T. D. Bennett and S. Horike, *Nat. Rev. Mater.*, 2018, **3**, 431–440.
4 R. Freund, O. Zaremba, G. Arnauts, R. Ameloot, G. Skorupskii, M. Dincă, A. Bavykina, J. Gascon,

A. Ejsmont, J. Goscianska, *et al.*, *Angew. Chem., Int. Ed.*, 2021, **60**, 23975–24001.
5 E. Barea, C. Montoro and J. A. Navarro, *Chem. Soc. Rev.*, 2014, **43**, 5419–5430.
6 B. Seoane, J. Coronas, I. Gascon, M. E. Benavides, O. Karvan, J. Caro, F. Kapteijn and J. Gascon, *Chem. Soc. Rev.*, 2015, **44**, 2421–2454.
7 B. Zhu, D. Wen, Z. Liang and R. Zou, *Coord. Chem. Rev.*, 2021, **446**, 214119.
8 S. Mubarak, D. Dhamodharan, P. N. Ghoderao and H.-S. Byun, *Coord. Chem. Rev.*, 2022, **471**, 214741.
9 W. Xia, A. Mahmood, R. Zou and Q. Xu, *Energy Environ. Sci.*, 2015, **8**, 1837–1866.
10 Q. Gan, H. He, K. Zhao, Z. He and S. Liu, *J. Colloid Interface Sci.*, 2018, **530**, 127–136.
11 J. Jin, Y. Zheng, S.-Z. Huang, P.-P. Sun, N. Srikanth, L. B. Kong, Q. Yan and K. Zhou, *J. Mater. Chem. A*, 2019, **7**, 783–790.
12 K. Wada, K. Sakaushi, S. Sasaki and H. Nishihara, *Angew. Chem., Int. Ed.*, 2018, **57**, 8886–8890.
13 T. Mehtab, G. Yasin, M. Arif, M. Shakeel, R. M. Korai, M. Nadeem, N. Muhammad and X. Lu, *J. Energy Storage*, 2019, **21**, 632–646.
14 X. Shen, H. Liu, X.-B. Cheng, C. Yan and J.-Q. Huang, *Energy Storage Mater.*, 2018, **12**, 161–175.
15 A. Manthiram, X. Yu and S. Wang, *Nat. Rev. Mater.*, 2017, **2**, 1–16.
16 D. Zhang, Z. Liu, Y. Wu, S. Ji, Z. Yuan, J. Liu and M. Zhu, *Adv. Sci.*, 2022, **9**, 2104277.
17 J. Qian, Y. Li, M. Zhang, R. Luo, F. Wang, Y. Ye, Y. Xing, W. Li, W. Qu and L. Wang, *Nano Energy*, 2019, **60**, 866–874.
18 P. Bai, J. Li, F. R. Brushett and M. Z. Bazant, *Energy Environ. Sci.*, 2016, **9**, 3221–3229.
19 J. Yun, B.-K. Park, E.-S. Won, S. H. Choi, H. C. Kang, J. H. Kim, M.-S. Park and J.-W. Lee, *ACS Energy Lett.*, 2020, **5**, 3108–3114.
20 Y. Xu, L. Gao, L. Shen, Q. Liu, Y. Zhu, Q. Liu, L. Li, X. Kong, Y. Lu and H. B. Wu, *Matter*, 2020, **3**, 1685–1700.
21 L. Fan, Z. Guo, Y. Zhang, X. Wu, C. Zhao, X. Sun, G. Yang, Y. Feng and N. Zhang, *J. Mater. Chem. A*, 2020, **8**, 251–258.
22 N. Contreras-Pereda, S. Pané, J. Puigmartí-Luis and D. Ruiz-Molina, *Coord. Chem. Rev.*, 2022, **460**, 214459.
23 L. S. Xie, G. Skorupskii and M. Dincă, *Chem. Rev.*, 2020, **120**, 8536–8580.
24 R. Makiura, *Coord. Chem. Rev.*, 2022, **469**, 214650.
25 V. Rubio-Giménez, M. Galbiati, J. Castells-Gil, N. Almora-Barrios, J. Navarro-Sánchez, G. Escorcia-Ariza, M. Mattera, T. Arnold, J. Rawle and S. Tatay, *Adv. Mater.*, 2018, **30**, 1704291.
26 P. Mao, H. Fan, C. Liu, G. Lan, W. Huang, Z. Li, H. Mahmoud, R. Zheng, Z. Wang and H. Sun, *Sustainable Energy Fuels*, 2022, **6**, 4075–4084.
27 L. Guo, J. Sun, W. Zhang, L. Hou, L. Liang, Y. Liu and C. Yuan, *ChemSusChem*, 2019, **12**, 5051–5058.
28 S. Gu, Z. Bai, S. Majumder, B. Huang and G. Chen, *J. Power Sources*, 2019, **429**, 22–29.
29 M. Parchine, J. McGrath, M. Bardosova and M. E. Pemble, *Langmuir*, 2016, **32**, 5862–5869.
30 T. L. Barr and S. Seal, *J. Vac. Sci. Technol., A*, 1995, **13**, 1239–1246.
31 T. Ohata, A. Nomoto, T. Watanabe, I. Hirosawa, T. Makita, J. Takeya and R. Makiura, *ACS Appl. Mater. Interfaces*, 2021, **13**, 54570–54578.
32 X. Wang, X. Ma and D. Zang, *Soft Matter*, 2013, **9**, 443–453.
33 L. S. Boucheron, J. T. Stanley, Y. Dai, S. S. You, C. T. Parzyck, S. Narayanan, A. R. Sandy, Z. Jiang, M. Meron and B. Lin, *Phys. Rev. E*, 2018, **97**, 052803.
34 A. Maestro, H. M. Hilles, F. Ortega, R. G. Rubio, D. Langevin and F. Monroy, *Soft Matter*, 2010, **6**, 4407–4412.
35 A. Dhanabalan, D. T. Balogh, A. Riul Jr., J. A. Giacometti and O. Oliveira Jr., *Thin Solid Films*, 1998, **323**, 257–264.
36 H. Morgan, D. M. Taylor and O. N. Oliveira Jr., *Biochim. Biophys. Acta, Biomembr.*, 1991, **1062**, 149–156.
37 J. Davies, *J. Colloid Sci.*, 1956, **11**, 377–390.
38 M. Hmadeh, Z. Lu, Z. Liu, F. Gándara, H. Furukawa, S. Wan, V. Augustyn, R. Chang, L. Liao and F. Zhou, *Chem. Mater.*, 2012, **24**, 3511–3513.
39 A. Mähringer, A. C. Jakowetz, J. M. Rotter, B. J. Bohn, J. K. Stolarczyk, J. Feldmann, T. Bein and D. D. Medina, *ACS Nano*, 2019, **13**, 6711–6719.
40 E. Sucre-Rosales, R. Fernandez-Teran, N. Urdaneta, F. E. Hernandez and L. Echevarria, *Chem. Phys.*, 2020, **537**, 110854.
41 M. Ko, L. Mendecki, A. M. Eagleton, C. G. Durbin, R. M. Stolz, Z. Meng and K. A. Mirica, *J. Am. Chem. Soc.*, 2020, **142**, 11717–11733.
42 H. Wu, W. Zhang, S. Kandambeth, O. Shekhah, M. Eddaoudi and H. N. Alshareef, *Adv. Energy Mater.*, 2019, **9**, 1900482.
43 R. Dong, M. Pfeffermann, H. Liang, Z. Zheng, X. Zhu, J. Zhang and X. Feng, *Angew. Chem., Int. Ed.*, 2015, **54**, 12058–12063.
44 M. de Lourdes Gonzalez-Juarez, C. Morales, J. I. Flege, E. Flores, M. Martin-Gonzalez, I. Nandhakumar and D. Bradshaw, *ACS Appl. Mater. Interfaces*, 2022, **14**, 12404–12411.
45 A. Urtizberea, E. Natividad, P. J. Alonso, M. A. Andrés, I. Gascón, M. Goldmann and O. Roubeau, *Adv. Funct. Mater.*, 2018, **28**, 1801695.
46 L. Fan, Z. Li, Z. Xu, K. Wang, J. Wei, X. Li, J. Zou, D. Wu and H. Zhu, *AIP Adv.*, 2011, **1**, 032145.
47 Q. Jiang, P. Xiong, J. Liu, Z. Xie, Q. Wang, X. Q. Yang, E. Hu, Y. Cao, J. Sun and Y. Xu, *Angew. Chem., Int. Ed.*, 2020, **59**, 5273–5277.
48 S. Maiti, A. Pramanik, U. Manju and S. Mahanty, *Microporous Mesoporous Mater.*, 2016, **226**, 353–359.
49 J. Park, M. Lee, D. Feng, Z. Huang, A. C. Hinckley, A. Yakovenko, X. Zou, Y. Cui and Z. Bao, *J. Am. Chem. Soc.*, 2018, **140**, 10315–10323.
50 Z. Wu, D. Adekoya, X. Huang, M. J. Kiefel, J. Xie, W. Xu, Q. Zhang, D. Zhu and S. Zhang, *ACS Nano*, 2020, **14**, 12016–12026.

51 S. Mutahir, C. Wang, J. Song, L. Wang, W. Lei, X. Jiao, M. A. Khan, B. Zhou, Q. Zhong and Q. Hao, *Appl. Mater. Today*, 2020, **21**, 100813.
52 J. Wang, J. Polleux, J. Lim and B. Dunn, *J. Phys. Chem. C*, 2007, **111**, 14925–14931.
53 A. C. Gómez-Herrero, C. Sánchez-Sánchez, F. Chérioux, J. I. Martínez, J. Abad, L. Floreano, A. Verdini, A. Cossaro, E. Mazaleyrat and V. Guisset, *Chem. Sci.*, 2021, **12**, 2257–2267.
54 M. S. Kim, J.-H. Ryu, D. Deepika, Y. R. Lim, I. W. Nah, K.-R. Lee, L. A. Archer and W. I. Cho, *Nat. Energy*, 2018, **3**, 889–898.
55 J. Xiao, Q. Li, Y. Bi, M. Cai, B. Dunn, T. Glossmann, J. Liu, T. Osaka, R. Sugiura, B. Wu, J. Yang, J.-G. Zhang and M. S. Whittingham, *Nat. Energy*, 2020, **5**, 561–568.
56 G. M. Hobold, J. Lopez, R. Guo, N. Minafra, A. Banerjee, Y. S. Meng, Y. Shao-Horn and B. M. Gallant, *Nat. Energy*, 2021, **6**, 951–960.
57 J. Man, W. Liu, H. Zhang, K. Liu, Y. Cui, J. Yin, X. Wang and J. Sun, *J. Mater. Chem. A*, 2021, **9**, 13661–13669.
58 G. Wang, P. He and L. Z. Fan, *Adv. Funct. Mater.*, 2021, **31**, 2007198.
59 G. Jiang, K. Li, F. Yu, X. Li, J. Mao, W. Jiang, F. Sun, B. Dai and Y. Li, *Adv. Energy Mater.*, 2021, **11**, 2003496.